

Implicit Surface Boundary Conditions for Blowing, Equilibrium Composition, and Diffusion-limited Oxidation

Matthew MacLean¹
CUBRC / LENS, Buffalo, NY 14225

Michael Barnhardt²
ELORET Corp, Sunnyvale, CA 94086

Michael Wright³
NASA Ames Research Center, Moffett Field, California 94035

Several models governing simplified gas/surface interaction have been developed and implemented in the DPLR code that governs catalytic recombination and blowing effects. The models include explicit blowing of arbitrary species mixtures from the surface, equilibrium catalytic recombination employing free-energy minimization, and diffusion limited oxidation of thermal protection system constituents. These models have been implemented in a tightly-coupled, implicit manner into the code to maintain robust stability and convergence at large time-steps. Several examples of the behavior of these models have been used to demonstrate the stability of the methods.

Nomenclature

A	cone area	\bar{F}	dimensionless blowing rate
b_k^0	initial elemental composition	\dot{w}	catalytic source term
c	mass fraction	α	stoichiometric coefficient
D_m	diffusion coefficient of species m	η	mole-mass ratio
h	enthalpy	Λ	Lagrange multiplier
\dot{m}	blowing mass flow rate	μ_j^0	specific Gibbs free-energy
M	molecular weight	ρ	density
\hat{n}	wall normal unit vector	ϕ	generic degree of freedom
P	pressure	<u>subscripts</u>	
R	universal gas constant	B	cone base area
k	thermal conductivity, Boltzmann constant	P	wetted porous area
q	wall heat transfer	W	wall location
T	temperature	1	located at near-wall cell center
U	velocity		

I. Introduction

ACCURATE prediction of the heating environment for reentry into Earth, Mars, and other planetary atmospheres from orbit or deep space requires accurate modeling of the complex interaction between the shock-layer gas and the surface of the thermal protection system (TPS) heat shield material. In most reentry applications, the TPS ablates during the descent to relieve the intense convective heat load on the vehicle and to protect the payload. The modeling of the gas/surface interaction at the interface is a first-order effect on the net level of heating experienced and must incorporate the effects of blowing due to gaseous material being injected into the flow, catalytic reactions resulting in changes to the chemical composition of the gas phase species near the surface, and chemical reactions between gas and TPS phase species.

¹ Senior Research Scientist; Senior Member AIAA; maclean@cubrc.org.

² Research Scientist; Member AIAA; michael.d.barnhardt@nasa.gov.

³ Senior Research Scientist; Associate Fellow AIAA.

In this work, we present several developments to the NASA Ames Research Center Data Parallel Line Relaxation (DPLR) code to enable and validate this type of analysis with an emphasis on fully-implicit coupling to the gas phase flow solver in order to maintain numerical stability and rapid convergence. In particular, three boundary conditions have been implemented and verified in the source code to target (1) wall normal blowing, (2) equilibrium chemical composition using free-energy minimization, and (3) diffusion-limited oxidation of TPS materials. The successful verification of these three fundamental, component boundary conditions have been used to demonstrate the implicit stability of DPLR as a step toward developing generalized finite-rate gas/surface interaction and implicitly coupled material response.

II. Numerical Code

The primary CFD tool used is the DPLR code provided by NASA Ames Research Center. DPLR is a multi-block, structured, finite-volume code that solves the reacting Navier-Stokes equations including finite rate chemistry and finite rate vibrational non-equilibrium effects. This code is based on the data-parallel line relaxation method¹ and implements a modified (low dissipation) Steger-Warming flux splitting approach² for the convection terms and central differencing for the diffusion terms. Finite rate vibrational relaxation is modeled via a simple harmonic oscillator vibrational degree of freedom³ using the Landau-Teller model⁴. Vibrational energy relaxation rates are computed by default from the semi-empirical expression due to Millikan and White⁵, but rates from the work of Camac⁶ and Park, et al⁷ are substituted for specific collisions where experimental data exists. Vibration-dissociation coupling is currently modeled using the $T-T_v$ approach of Park⁸ or with some preliminary implementation of CVDV coupling⁹. Transport properties are appropriately modeled in DPLR for high enthalpy flow^{10,11} using the binary collision-integral based mixing rules from Gupta, et al¹². Diffusion coefficients are modeled using the self-consistent effective binary diffusion (SCEBD) method¹³. Turbulence models available in the DPLR code currently include the Baldwin-Lomax 0-equation model¹⁴, the Spalart-Allmaras model 1-equation model¹⁵, and the Shear Stress Transport (SST) 2-equation model¹⁶ each with corrections for compressibility effects^{17,18}. Recent relevant capabilities of the DPLR code involve automated grid adaptation to improve solution quality¹⁹.

Surface boundary conditions in DPLR are imposed implicitly, which means that the boundary condition is written in the general form given in Eqn (1).

$$\Delta^n \phi_w = [A] \Delta^n \phi_1 + [B] \Delta^n \phi_2 + [C] \quad (1)$$

The coefficients of the matrices A and B are composed of the Jacobians of the explicit form of the boundary condition. By utilizing the Jacobian contributions of the boundary condition in the iterative solution of the interior, greatly enhanced convergence rates and better stability of the solver can be achieved. For a simple Dirichlet or Neumann boundary, casting the boundary condition in this form is trivial, but, for complex systems, obtaining accurate Jacobian contributions can be challenging.

III. Simulations with Surface Blowing

As a pre-cursor to the more detailed surface interaction models, the wall-normal, blowing capability of DPLR has been validated. In previous versions of the DPLR code, convergence issues were sometimes encountered with certain combinations of specified blowing rates and specified species compositions. These combinations often required several orders of magnitude more iterations to obtain the same level of convergence than for a similar non-blowing case. A modification of the implicit structure of the Jacobian matrix eliminated this issue and has allowed us to blow arbitrary gas mixtures from the surface with no significant convergence penalty.

A. Generic Cone with Blowing

To demonstrate this improved capability, three separate cases have been considered with a 10° half-angle cone with a blunt nose. Freestream conditions for the problem were selected as $U = 4.0$ km/s, $\rho = 0.05$ kg/m³, $T = 200$ K, and undisturbed air. The first case is for a non-blowing smooth wall. The second case specifies uniform mass blowing at a rate of 0.25 kg/m²-s over the entire surface. The surface for this case is considered non-catalytic, which means that the composition of the blowing gas is the composition of the air mixture implied for zero mass fraction gradients of all species. At the freestream conditions specified, this gas is mostly atomic oxygen and molecular nitrogen with a small amount of nitric oxide as is found in the inviscid shocklayer. The third case was run with the same mass flow rate as the second, but the composition was specified to be 100% carbon monoxide (CO). The mole fraction of CO is shown in Fig 1 for cases two and three.

The blowing velocity for all cases is shown in Fig 2. Since the mass flow rate is specified constant, the blowing velocity varies from point to point on the body based on the changing surface density. It is also different for cases two and three because of the different mass composition of the blowing gases in these cases.

The residual for these three cases is plotted in Fig 3. Although the smooth wall case converges most quickly of the three, the other two cases converge to machine zero in a similar number of iterations, taking as little as 50% longer. This is considerably improved from previous versions and is a result of the improved coupling of the boundary condition into the flow. The demonstration of blowing from the surface is a significant step toward the diffusion limited oxidation response model where blowing must be coupled to species production rates.

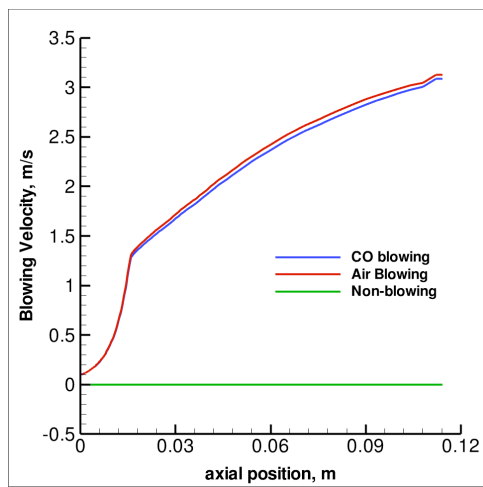


Figure 2. Wall Normal Blowing velocity with CO Blowing and Air (Non-catalytic) Blowing Rates of 0.25 kg/m²-s

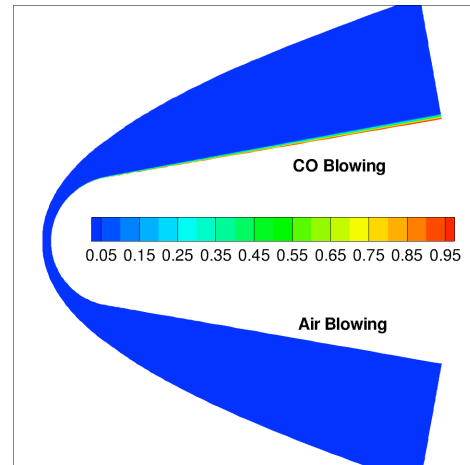


Figure 1. Carbon Monoxide (CO) Mole Fraction Contours for Cases with CO Blowing and Air (Non-catalytic) Blowing Rates of 0.25 kg/m²-s

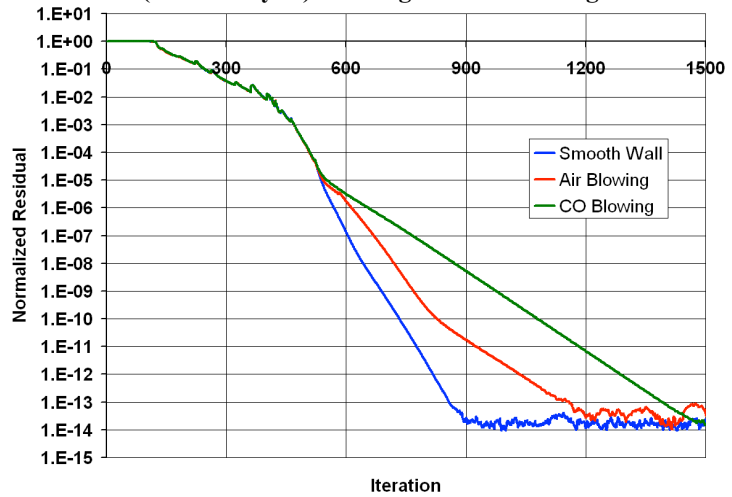


Figure 3. Convergence of Blowing and Non-blowing Cone Cases

B. Blowing Study by Marvin and Akin²⁴

To validate against some experimental data, comparisons with a series of blowing experiments performed by Marvin and Akin²⁴ have been made. These experiments measured heat transfer along a 5° half-angle cone with a field of discrete porous holes through which air, argon, and helium were blown at nearly constant injection flow rates. The nominal freestream Mach number of 7.4 and Reynolds number based on cone length of 4.7x10⁶ were provided. The grid employed and the computed Mach contour field is shown in Fig 4. The cone model had a sharp tip with an upstream section of non-blowing surface that is shown in gray, followed by a section with blowing shown in red. Total length of the cone was reported to be 50-cm with 9.5-cm of non-blowing upstream length, where the dimensions are surface distance on the cone (not axial). The boundary layer entered the blowing zone laminar in all cases, though transition due to the instability induced by the blowing was observed in the middle of the blowing region in most cases.

The cases with air blowing into air are considered first. Per the format of Marvin and Akin, the blowing rate is non-dimensionalized with the symbol \bar{F} , which they define as $\bar{F} = 1.3\dot{m}A_p / \rho_\infty U_\infty A_B$. Using the constants provided by Marvin and Akin, the value of this blowing parameter may be computed as $\bar{F} = (0.3296 \text{ m}^2\text{s/kg})\dot{m}$. Values of \bar{F} listed are given as percentages. The measured and computed heat transfer levels are also non-dimensionalized by the measured value of heating just at the front edge of the bowing section. This reference value is 1.66 W/cm².

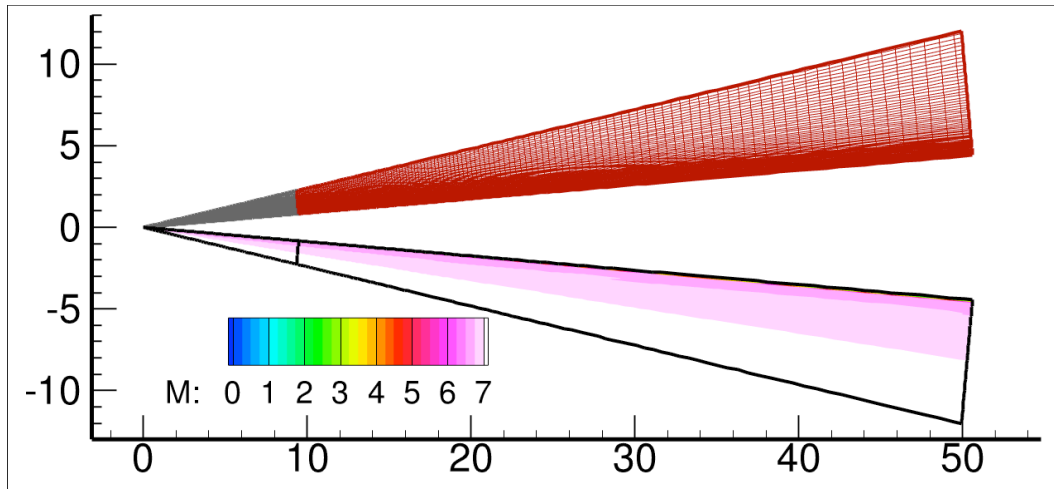


Figure 4. Grid and Mach Number Contours for Marvin and Akin 5° Half-Angle Cone (Dimensions in cm)

The comparison with the measured data for the non-blowing baseline and three levels of air blowing are shown in Fig 5(a) (which compares exactly with Fig 7a in the original reference). For all the cases, the flow transitions experimentally mid-way down the porous section as indicated by the rapid increase in heat transfer in the plots of the original paper. Since we are only concerned with validating the blowing conditions under laminar flow here, any experimental points downstream of the transition onset have been eliminated. Overall, the agreement in the remaining laminar region may be considered to be generally good. It is interesting that the largest discrepancy is with the baseline case with no blowing. Since only a nominal freestream condition was available that was the same for all runs, this discrepancy may possibly be due to run-to-run variation in the experiments or to other unknown causes since the information about the experiments is limited. In any case, the blowing cases are of primary interest and the agreement with those is better. Convergence behavior is plotted in Fig 5(b). Larger blowing rates take longer to converge, but it should be noted that at the highest two blowing rates, the laminar boundary layer at the downstream end of the cone (occurring at approximately $S=3.0$) is separated (the experiments transitioned upstream of this region), so the slow convergence rate is at least in part due to that rather than the blowing boundary condition explicitly. The convergence behavior is consistent with earlier versions of the CFD code since this series uses air injection into an air boundary layer.

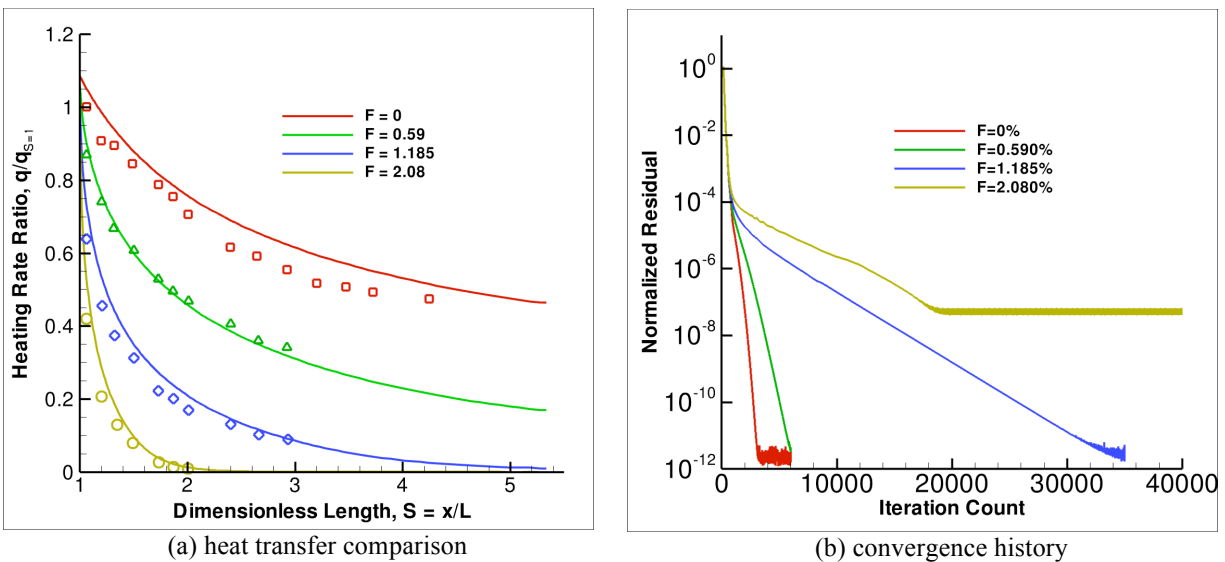


Figure 5. Heat Transfer Comparison and Solution Convergence History with Air Injectant Gas

Injection with other gases is considered next in Fig 6(a) for argon injection and Fig 6(b) for helium injection. The dimensionless blowing parameter and the dimensionless heat transfer measurements are defined in exactly the

same way as for the air cases. The non-blowing case is the same one as shown from Fig 5(a). Initially, the results for both argon and helium seem quite incorrect. The argon results show that the predicted heat transfer is significantly higher than the data for all cases with argon blowing. In contrast, the predicted helium heating patterns are significantly lower than the measured values. In fact, the predicted heating to the surface is actually negative, meaning that energy is removed from the surface rather than added to it.

The reason for the observation of seemingly poor heating prediction for these gases may be considered further by considering the definition of heat transfer used in Fig 6 which is given in Eqn (2) (neglecting work done by shear stress which is very small in this case).

$$q_W = -k(\nabla T \cdot \hat{n}) - \sum_{m=1}^{ns} \rho D_m (h_{s,m} + h_{c,m}) (\nabla c_m \cdot \hat{n}) \quad (2)$$

This definition is actually an *energy flux* passing through the semi-solid surface from the gas phase domain into the solid domain of the cone. Here, the first term is the convective heating due to thermal gradients, and the second term is the energy carried across the boundary by diffusion, where the enthalpy is from both the sensible and the chemical contributions. If the surface in question is the boundary between a gas and a solid surface, then the energy (heat) delivered to the surface is equal to this energy flux defined in Eqn (2).

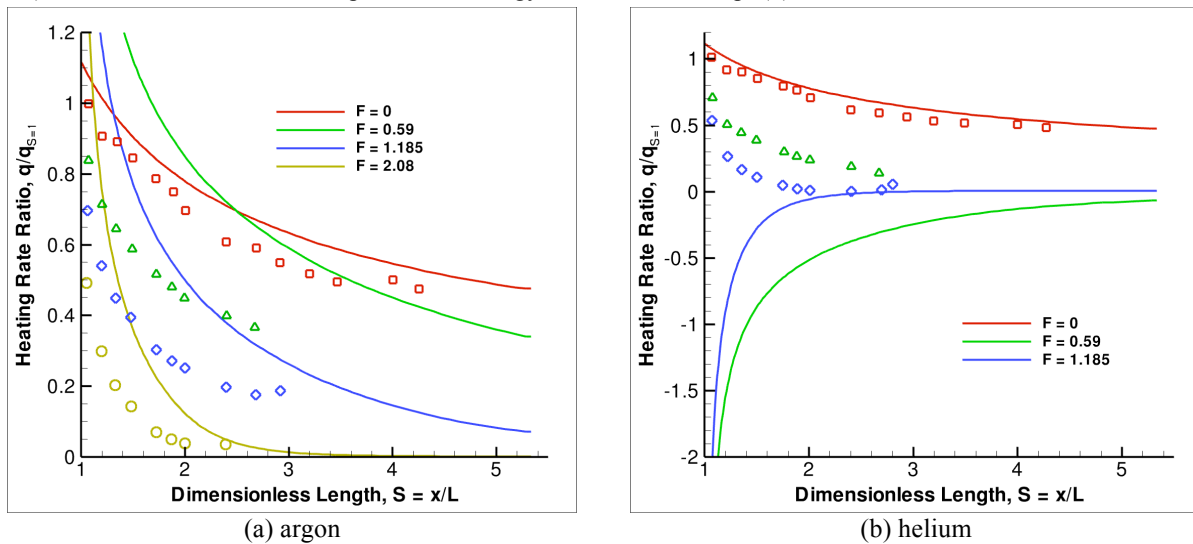


Figure 6. Heat Transfer Comparison Argon and Helium Injectant Gases using Eqn (2)

In the case of the Marvin and Akin experiments, the large negative energy flux observed with the helium blowing cases comes from the second term in Eqn (2). This is the term responsible for “catalytic” heating on solid surfaces where catalytic production boundary conditions are employed. The change in heat of formation between species diffusing to the surface and those diffusing away from the surface results in additional energy flux into the solid. However, in this particular case, the heat of formation of all species (N_2 , O_2 , He) is defined to be zero. The sensible enthalpy, which can be thought of as a specific heat times a surface temperature for each species, is significantly larger for helium than for air by a factor of 5.20 per unit mass. The helium diffusing away from the surface is such an effective carrier of energy that the removal by this mechanism is larger than the energy transmitted to the surface by thermal diffusion. The total heat transfer to the surface is predicted to be negative.

The proper definition of heat transfer as measured in the experiments when the surface is semi-porous as in the experiments of Marvin and Akin is much less clear. One potential issue that has been considered is the fact that the helium, which is such an efficient remover of energy, does not originate within the wall of the cone. It is brought in from a reservoir through a plumbing system into the surface of the cone and then blown out into the boundary layer. Therefore, one possible explanation for the behavior of the predicted heat transfer with helium and argon is that, since the injectant gas enters and leaves the surface domain with the same species enthalpy, the fourth term in Eqn (2) should not be counted toward the heat delivered to the effective surface. This energy enters and leaves the near-surface region for a net effect of zero. If this change is made, the predicted heat transfer compares to the experiments for argon and helium injectant gases as shown in Fig 7. The agreement for both gases is significantly improved since the mass-specific heat capacity of argon is less than for air and it is greater for helium than for air.

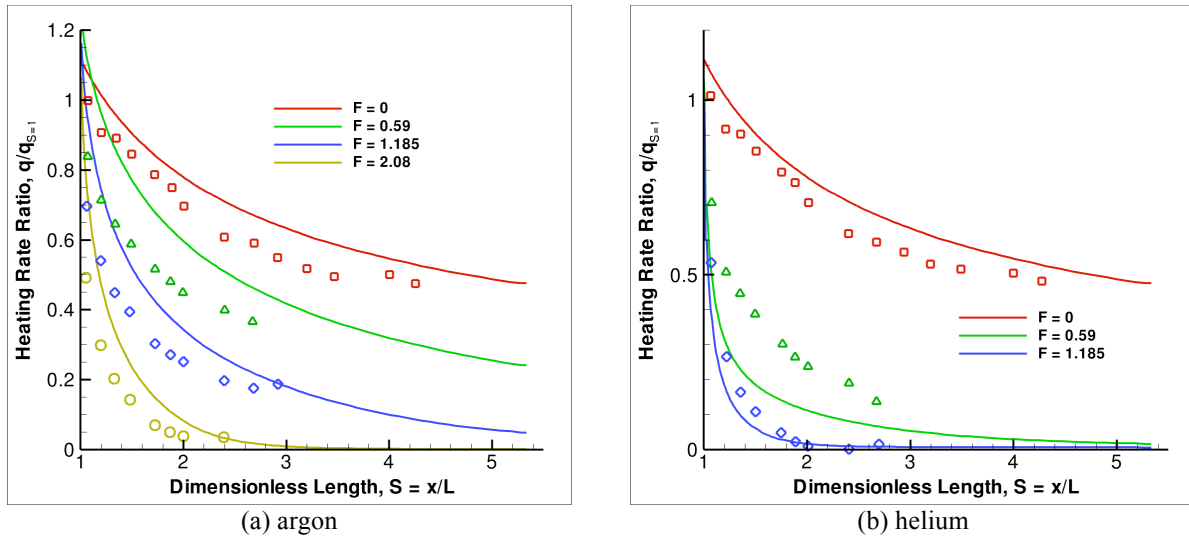


Figure 7. Heat Transfer Comparison Argon and Helium Injectant Gases Neglecting Term #2 of Eqn (2)

The improved agreement may lend credibility to this potential accounting of energy, but it is clear that, for blowing experiments like this one, it is necessary to be very careful about documenting how the experimental measurements were made. Issues such as conduction between the surface and the injectant gas in the plenum chamber and through the orifice system must be considered. Unfortunately, the information about this set of experiments is limited.

In any case, the numerical stability of the code and its ability to blow injectant gases not present in the freestream is the primary focus of this work. The convergence history of the cases with argon injection and helium injection is shown in Fig 8. Here again, we observe that the convergence rate decreases some with increased blowing rate, but it is not slowed unreasonably by the blowing boundary condition. In fact, by comparing these convergence results to the residual obtained with the air simulations in Fig 5(b), we observe that, if anything, the argon and helium cases converge faster. Again, the laminar boundary layer at the trailing surface of the cone is separated for the $F=2.08\%$ case with argon injection. Validation of the boundary condition for a non-reactive, specified blowing rate has been considered a necessary first step toward validating integrated surface and material response boundaries in the remaining sections of this and future developments of the DPLR code.

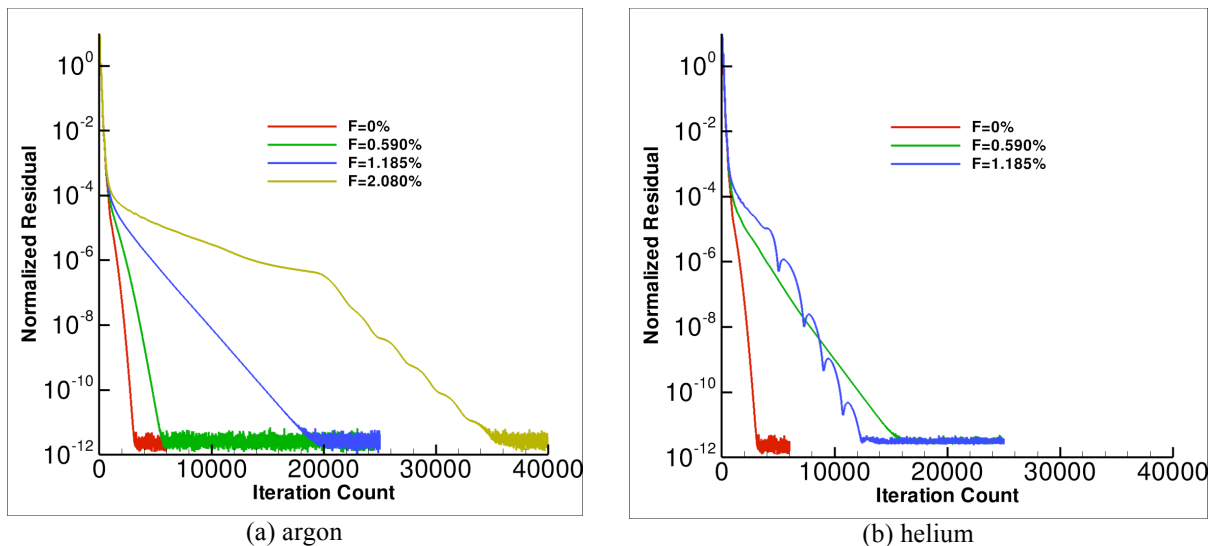


Figure 8. Convergence History of Solver with Cases Blowing Argon and Helium Injectant Gases

IV. Simulation of Surface Equilibrium Composition with Free-energy Minimization

A. Equilibrium Composition Free-energy Minimization Algorithm

The computation of the equilibrium composition of any gas mixture as a function of two thermodynamic state variables has been performed using the Gibbs free-energy minimization technique of Gordon and McBride²⁵. This is the same technique that is utilized in the CEA code. Their technique casts the composition of the system in terms of mole-mass ratio and employs the natural log of all variables in the system, which ensures very robust convergence.

The Gibbs system consists of a Gibbs energy equation for each species, given in Eqn (3),

$$\left(\frac{\mu_j^0}{RT}\right) + \ln\left(\frac{\eta_j}{\eta}\right) + \ln\left(\frac{P}{P_{REF}}\right) + \sum_{k=1}^{NE} \alpha_{kj} \Lambda_k = 0 \quad (3)$$

a total mass equation, given in Eqn (4),

$$\sum_{j=1}^{NS} \eta_j - \eta = 0 \quad (4)$$

and one or more elemental conservation constraints enforced using LaGrange multipliers given in Eqn (5).

$$\sum_{j=1}^{NS} \alpha_{kj} \eta_j - b_k^0 = 0 \quad (5)$$

The system given in Eqns (3), (4), and (5) is iterated to convergence using Newton iteration. The system is quite robust and converges rapidly, usually in 20 – 30 iterations. Convergence is slower at low temperatures and pressures, but application of limiting as described by Gordon and McBride has produced robust convergence at all conditions and chemical systems studied. The CEA code performs a substitution step and solves a reduced set of equations that are equal to the number of elemental constraints plus one. In this way, CEA can solve for a very large number of chemical species without a significant increase in overhead. For application to gas phase aerothermodynamics, the number of chemical species involved is usually on the order of 10, so the reduction step was not employed. The system solved is given in Eqn (6).

$$\begin{bmatrix} 1 & 0 & \dots & 0 & -1 & a_{1,1} & \dots & a_{p,1} \\ 0 & 1 & \dots & 0 & -1 & a_{1,2} & \dots & a_{p,2} \\ \vdots & \vdots & \ddots & \vdots & \vdots & \vdots & \ddots & \vdots \\ 0 & 0 & \dots & 1 & -1 & a_{1,N} & \dots & a_{p,N} \\ \eta_1 & \eta_2 & \dots & \eta_N & \eta & 0 & \dots & 0 \\ a_{1,1}\eta_1 & a_{1,2}\eta_2 & \dots & a_{N,1}\eta_N & 0 & 0 & \dots & 0 \\ \vdots & \vdots & \ddots & \vdots & \vdots & \vdots & \ddots & \vdots \\ a_{p,1}\eta_1 & a_{p,2}\eta_2 & \dots & a_{p,N}\eta_N & 0 & 0 & \dots & 0 \end{bmatrix} \begin{bmatrix} \Delta \ln(\eta_1) \\ \Delta \ln(\eta_2) \\ \vdots \\ \Delta \ln(\eta_N) \\ \Delta \ln(\eta) \\ \Delta \Lambda_1 \\ \vdots \\ \Delta \Lambda_p \end{bmatrix} = \begin{bmatrix} -\left(\frac{\mu_1^0}{RT}\right) - \ln\left(\frac{\eta_1}{\eta}\right) - \ln\left(\frac{P}{P^0}\right) - \sum_{k=1}^p \alpha_{k,1} \Lambda_k \\ -\left(\frac{\mu_2^0}{RT}\right) - \ln\left(\frac{\eta_2}{\eta}\right) - \ln\left(\frac{P}{P^0}\right) - \sum_{k=1}^p \alpha_{k,2} \Lambda_k \\ \vdots \\ -\left(\frac{\mu_N^0}{RT}\right) - \ln\left(\frac{\eta_N}{\eta}\right) - \ln\left(\frac{P}{P^0}\right) - \sum_{k=1}^p \alpha_{k,N} \Lambda_k \\ \eta - \sum \eta_k \\ b_1^0 - \sum a_{1,k} \eta_k \\ \vdots \\ b_p^0 - \sum a_{p,k} \eta_k \end{bmatrix} \quad (6)$$

Data to obtain the Gibbs energy at standard state is also obtained from the extensive set of tables provided by Gordon and McBride²⁵. The tabulated data are smoothly varying functions of temperature, typically in the range of 200 – 20,000 K. A constant specific heat is assumed outside this range to preserve the continuity and avoid any convergence errors or erratic behavior during the early iterations.

Implicit coupling in DPLR is performed by solving the Gibbs energy system to convergence at each flow step. The equilibrium system is solved for the explicit, local surface pressure and temperature for each CFD flow iteration. The elemental constraints as well as the initial composition are set from the species diffusing to the surface from the near wall cell. The implicit (Jacobian) dependencies of the equilibrium surface composition on

pressure, temperature, and near wall species composition are needed to keep the system stable. These can be obtained by differentiating Eqns (3), (4), and (5) and solving the system one final time. This is exactly the same technique as employed by Gordon and McBride to obtain derivatives necessary to compute secondary parameters such as equilibrium sound speed and specific heat ratio. This system is given in Eqn (7).

$$\begin{bmatrix}
 1 & 0 & \cdots & 0 & -1 & a_{1,1} & \cdots & a_{P,1} \\
 0 & 1 & \cdots & 0 & -1 & a_{1,2} & \cdots & a_{P,2} \\
 \vdots & \vdots & \ddots & \vdots & \vdots & \vdots & \ddots & \vdots \\
 0 & 0 & \cdots & 1 & -1 & a_{1,N} & \cdots & a_{P,N} \\
 \eta_1 & \eta_2 & \cdots & \eta_N & \eta & 0 & \cdots & 0 \\
 a_{1,1}\eta_1 & a_{1,2}\eta_2 & \cdots & a_{1,N}\eta_N & 0 & 0 & \cdots & 0 \\
 \vdots & \vdots & \ddots & \vdots & \vdots & \vdots & \ddots & \vdots \\
 a_{P,1}\eta_1 & a_{P,2}\eta_2 & \cdots & a_{P,N}\eta_N & 0 & 0 & \cdots & 0
 \end{bmatrix}
 \begin{bmatrix}
 \partial(\ln\eta_1)/\partial q \\
 \partial(\ln\eta_2)/\partial q \\
 \vdots \\
 \partial(\ln\eta_N)/\partial q \\
 \partial(\ln\eta)/\partial q \\
 \partial(\Lambda_1)/\partial q \\
 \vdots \\
 \partial(\Lambda_P)/\partial q
 \end{bmatrix}
 =
 \begin{bmatrix}
 H_1^0/RT \\
 H_2^0/RT \\
 \vdots \\
 H_N^0/RT \\
 0 \\
 0 \\
 \vdots \\
 0
 \end{bmatrix}
 \text{OR}
 \begin{bmatrix}
 -1 \\
 -1 \\
 \vdots \\
 -1 \\
 0 \\
 0 \\
 \vdots \\
 0
 \end{bmatrix}
 \text{OR}
 \begin{bmatrix}
 0 \\
 0 \\
 \vdots \\
 0 \\
 0 \\
 a_{1,m} \\
 \vdots \\
 a_{P,m}
 \end{bmatrix}
 \quad (7)$$

The Jacobian of the system is the same as the one used to solve for the equilibrium composition in Eqn (6), so the same source code algorithm can be used to invert the Jacobian matrix one final time. The cost of obtaining all sets of derivatives is simply equal to a single matrix multiplication of the inverted Jacobian with different right-hand side vectors. Finally, the implicit boundary condition can be enforced in DPLR at each gas/surface cell face by using Eqn (8) with the equilibrium values and derivatives obtained from the equilibrium solver routine.

$$\Delta^n c_w = c_{EQ} - c_w + \frac{\partial c_{EQ}}{\partial T_w} \Delta^n T_w + \frac{\partial c_{EQ}}{\partial P_w} \Delta^n P_w + \sum \frac{\partial c_{EQ}}{\partial c_1} \Delta^n c_1 \quad (8)$$

B. Sphere-cone Flow in Carbon Dioxide with Radiative Equilibrium Wall

The first problem considered to validate the equilibrium composition boundary is a 70° sphere-cone with freestream conditions that might be representative of a Venus entry. The case is axisymmetric. The conditions selected are $U = 8.0$ km/s, $\rho = 0.002964$ kg/m³, $T = 200$ K, 100% CO₂, and the surface is assumed to be at radiative equilibrium with an emissivity of 0.85. At this energy level, the carbon dioxide readily dissociates in the shock-layer, and the wall is heated by convective heating to a temperature that is sufficiently high that (at equilibrium) the carbon dioxide does not completely recombine. Several shock layer properties are shown in Fig 9, including Mach number, temperature, and mass fraction of carbon monoxide. Inside the shock-layer, the gas exists mostly as carbon monoxide.

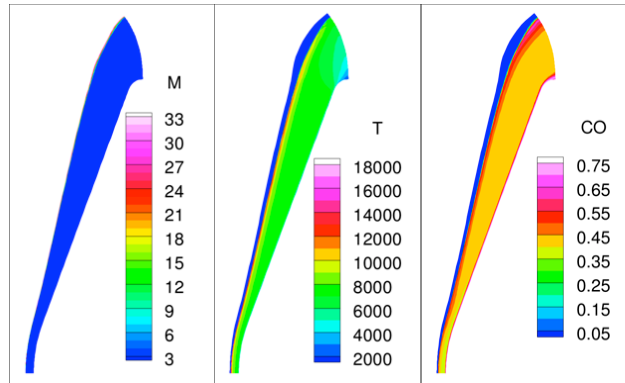


Figure 9. Shock Layer Mach Number, Temperature, and Carbon Monoxide (CO) for 70° Sphere-cone

The surface heat transfer of three different catalytic surface models is shown in Fig 10(a). The non-catalytic wall predicts the lowest level of heating while the super-catalytic model, enforcing complete recombination to CO₂, predicts a level of heating that is more than twice as much. The equilibrium boundary condition falls somewhere in between and predicts a level of heating that is more than the non-catalytic wall, but significantly less than the super-catalytic wall. This implies that partial recombination occurs, but the surface temperature is sufficiently high that the equilibrium state of the gas is not returned completely to CO₂. The surface temperature profiles are shown in Fig 10(b), and the equilibrium boundary is again observed to be mid-way between the other two solutions. For a surface this hot, where complete recombination is not physically plausible based on the condition of equilibrium, a savings of approximately 500K for the TPS design results from the application of a boundary condition that is more energetically appropriate than the super-catalytic wall. The surface pressure profiles (nominally constant for all

cases) are also given in Fig 10(b), so that the chemical state of the equilibrium boundary case varies from point to point based on the equilibrium composition at each given temperature and pressure pair.

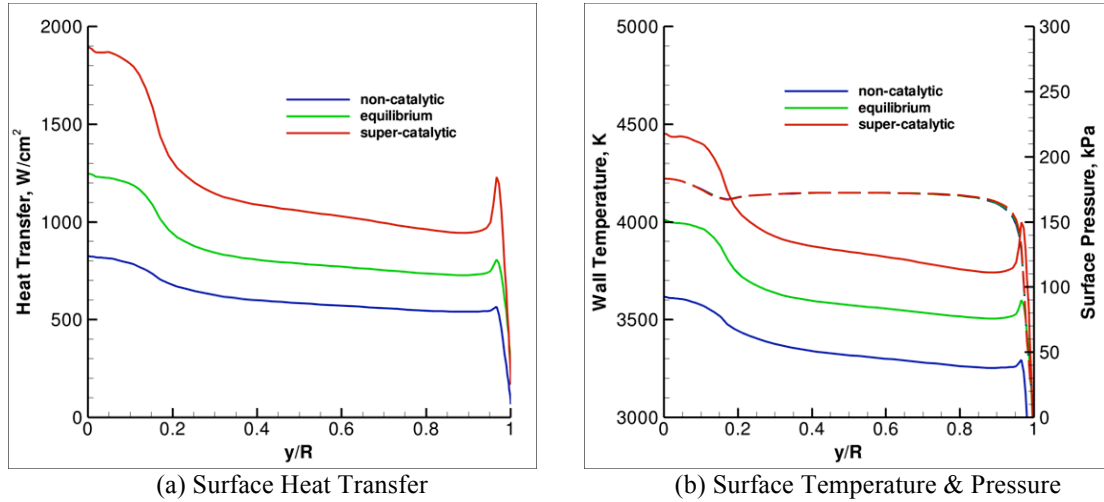


Figure 10. Surface Response using Non-catalytic, Super-catalytic, and Equilibrium Surface Models

The profiles of surface chemistry composition are shown in Fig 11 for the equilibrium surface boundary solution. As implied in the flowfield, much of the flow exists as carbon monoxide at these temperatures, although the composition does vary somewhat for different temperatures along the surface. Four points were selected at random at locations approximately evenly spaced along the surface and the temperature and pressure from Fig 10(b) was used to compute the equilibrium composition using the CEA code. These results are plotted for each species with the diamond symbols, and they agree exactly with the converged result from DPLR.

Finally, the issue of stability and convergence is considered for this case. The normalized residual for the three solutions with the non-catalytic, super-catalytic, and equilibrium catalytic boundary conditions is shown in Fig 12. The case with the equilibrium boundary exhibits slight start-up transient increase in residual, which may solely be an artifact of the normalization method (the residual in all cases is simply normalized by the value obtained from iteration one). The stability can be sensitive during the early part of the flow convergence because of the large changes in surface temperature that occur and a careful CFL ramp must be employed during the first few iterations. However, within two hundred iterations, the equilibrium boundary stabilizes and exhibits convergence behavior that is competitive with the simple Dirichlet and Neumann boundary conditions. The asymptotic rate of convergence and number of iterations required are approximately equal for all boundary conditions.

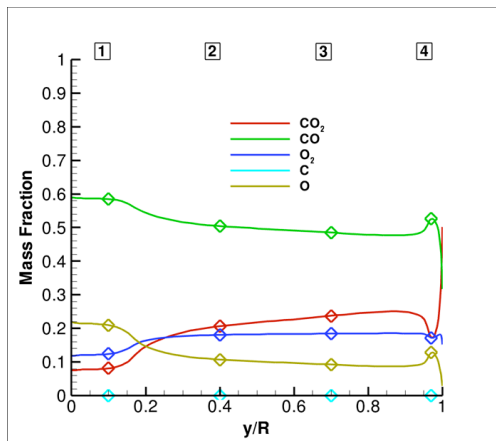


Figure 11. Chemical Composition along Surface of Sphere-cone with Equilibrium Surface Boundary and Comparison with CEA Code

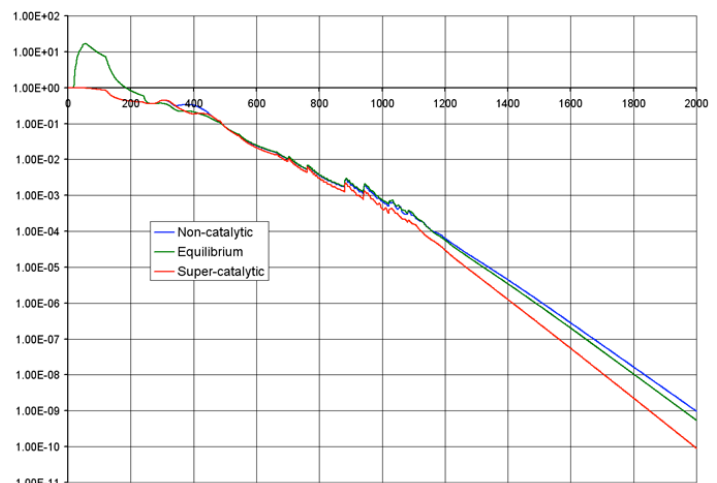


Figure 12. Normalized Residual for Sphere-cone Cases

C. Spherical Capsule in Air Flow with Radiative Equilibrium

For low energy conditions and/or cold walls, the equilibrium catalytic boundary condition should generate a completely recombined state that is energetically consistent with the super-catalytic boundary condition. This was tested with a lower speed air condition on a spherical capsule forebody that is geometrically similar to the Apollo or the upcoming CEV shapes. The conditions were chosen to be $U = 5.0 \text{ km/s}$, $\rho = 0.001 \text{ kg/m}^3$, $T = 200 \text{ K}$, and 79% $\text{N}_2/21\% \text{ O}_2$ by volume. The flowfield in the shock layer is shown in Fig 13, which gives contours of Mach number, temperature, and atomic oxygen. These freestream conditions were chosen to generate post-shock temperatures that are sufficiently high to completely dissociate the molecular oxygen in the shock layer, but to have a surface temperature that is below the point at which oxygen dissociation will occur even for the super-catalytic condition. The surface temperature profiles for the non-catalytic, super-catalytic, and equilibrium catalytic wall models are given in Fig 14. Here, unlike the previous case, the equilibrium and super-catalytic wall temperatures agree exactly as they should with a peak temperature at the stagnation point of approximately 1800K. At this temperature, the equilibrium state of oxygen is molecular and the equilibrium state of nitrogen is molecular. This result is verified with the predicted profiles of atomic oxygen on the surface for the three cases shown in Fig 15. For the non-catalytic wall case, the surface is composed primarily of atomic oxygen, but for the super-catalytic and equilibrium boundary cases, the surface contains no atomic oxygen. This result verifies that at low energies or cold wall, the equilibrium boundary decays to the trivial result as it should.

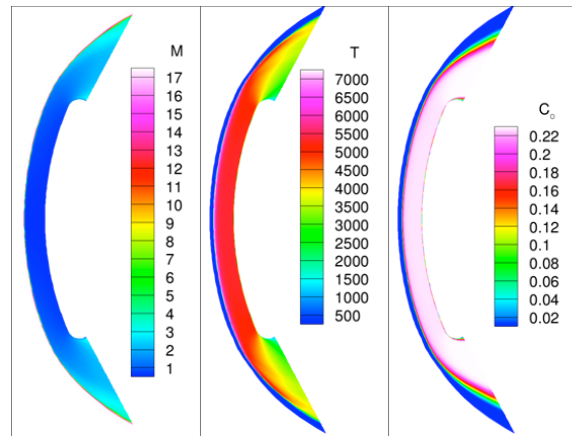


Figure 13. Shock Layer Mach Number, Temperature, and Atomic Oxygen (O) for Spherical Capsule

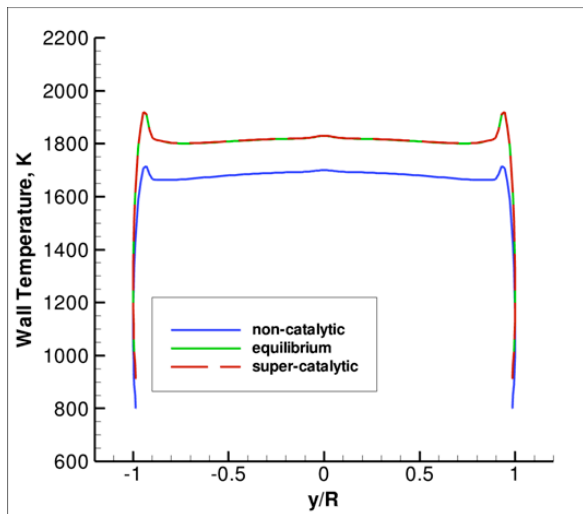


Figure 14. Surface Temperature Distributions over Spherical Capsule

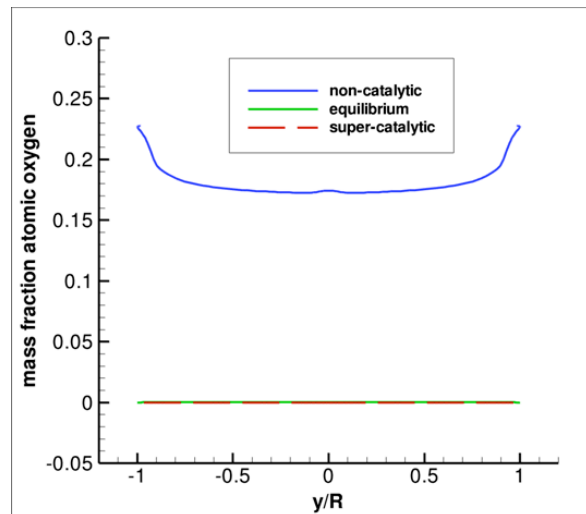


Figure 15. Mass Fraction of Atomic Oxygen over Surface of Spherical Capsule

D. Cone in Carbon Dioxide Flow with Radiative Equilibrium

Finally, a case is considered of a 10° half-angle cone with a 2.54-cm (1.0-inch) nose radius. Freestream conditions for this case were picked as $U = 6.0 \text{ km/s}$, $\rho = 0.001 \text{ kg/m}^3$, $T = 200 \text{ K}$, and 100% CO_2 . Under these conditions, the flow is highly dissociated in the nose region and relaxes on the frustum of the cone surface. The

surface temperature is likewise very high near the nose and much lower on the frustum. The Mach number contours of this flowfield are shown in Fig 16.

The surface heat transfer is plotted versus the normalized radial coordinate in Fig 17. Note that the heating is plotted on a log scale because it ranges over several orders of magnitude from the stagnation point to the cone. At the stagnation point, the equilibrium catalytic boundary shows a level of heating between the non-catalytic and super-catalytic solutions as it did in the first case. The reduction in heating from the super-catalytic solution is more significant than it may appear on the graph since it is nearly a factor of two smaller. The non-catalytic solution displays an undershoot effect just downstream of the nose ($y/R = 1.0$) because of nearly-frozen, dissociated chemistry that relaxes very

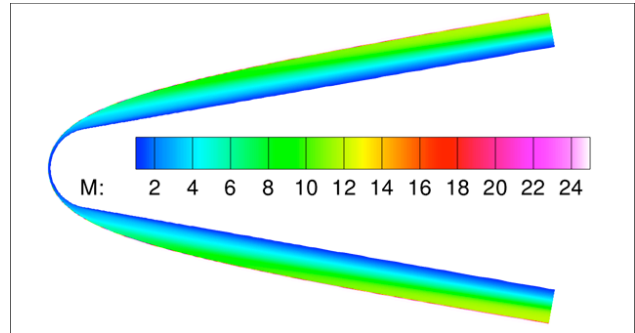


Figure 16. Mach Number Contours of Shock Layer of Cone Problem

slowly along the cone frustum. The equilibrium boundary solution, while showing a significantly lower heating in the stagnation region, asymptotes toward the super-catalytic heating level at the back of the cone. However, in a region downstream of the nose region from y/R of 1.0 to approximately 2.0, the heating level predicted by the equilibrium boundary condition slightly exceeds the super-catalytic heating result.

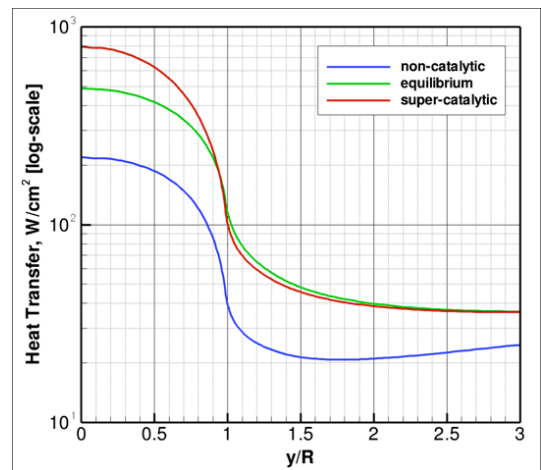


Figure 17. Surface Heat Transfer Profiles on Cone Problem

This seemed counter-intuitive at first, especially considering the distribution of the carbon dioxide species shown in Fig 18. At the location of y/R of 1.0, the wall temperature is high enough such that the carbon dioxide is still partially dissociated at the surface. Since the flow is not fully recombined at this station, there is less heating due to catalytic activity than the super-catalytic model; therefore, the convective heating must be higher for the equilibrium boundary than for the super-catalytic boundary to make up for this deficit. As was observed from the heat transfer profile in Fig 17, the non-catalytic wall reflects the nearly-frozen character of the flow and displays slow, steady increasing recombination toward CO_2 that is only partially completed at the end of the cone surface.

A closer examination of the boundary layer growth predicted by these three surface models on the cone is shown

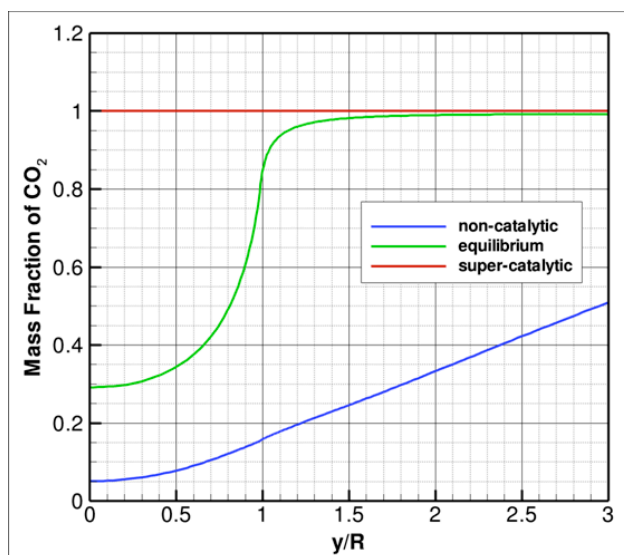


Figure 18. Surface Distribution of Carbon Dioxide Species on Cone

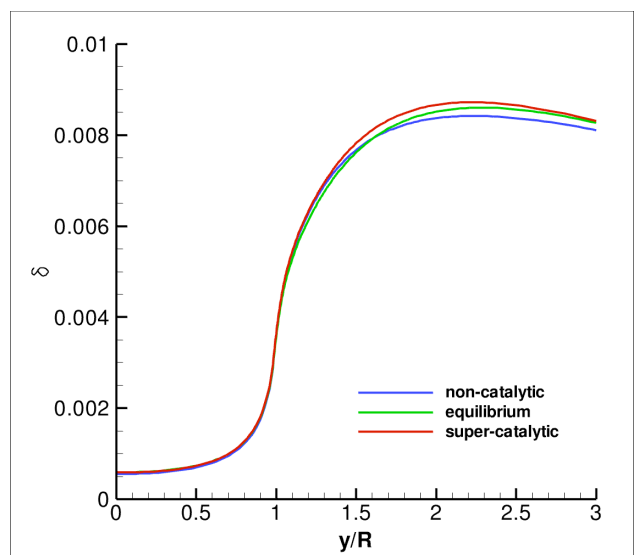


Figure 19. Predicted Boundary Layer Thickness for Three Catalytic Surface Models on the Cone Surface

in Fig 19. The equilibrium boundary has a slightly smaller boundary layer thickness than the super-catalytic model in the range from y/R of 1.0 to about 2.0, which explains the increased convective heat transfer observed along part of the cone surface downstream of the nose. The change to the boundary layer is caused by the dynamic rate of recombination from point to point along the cone nose that, in turn, affects the thermal and momentum boundary layers. Despite this, the equilibrium boundary condition predicts a significantly less costly design than the super-catalytic wall boundary condition does.

V. Simulation of Diffusion Limited Oxidation Material Response

A. Diffusion Limited Oxidation Model

A simplified material response model has also been implemented in the DPLR code where the rate of reaction is driven by the amount of a gaseous species diffusing to the surface. This type of model is a slightly generalized version of the carbon oxidation models used by Titov, et al²⁶ and Park²⁷. In DPLR, a boundary condition has been built for an oxidation reaction of the form given in Eqn (9).



The second reactant, $[S]$, is some TPS constituent that is determined by mass conservation between the gas phase products, B and C , and oxidizer, A . Most often, this form is employed for the reaction of carbon (C_S) with atomic oxygen (O) or molecular oxygen (O_2), but may be used for any TPS reaction fitting this form. The source code allows for any number of reactions of this form to be read into the solver through a convenient text file. The form of the reaction in Eqn (9) neglects any sort of backward rate, so the system does not adhere strictly to equilibrium, but, for many practical TPS cases, the oxidation mechanism can be so strong that the entire mechanism can be dominated by the rate at which oxidizer diffuses to the surface in this manner.

The production rate of each participant species from each reaction is computed using the mean thermal speed and is of the form given in Eqn (10).

$$\dot{w}_i = \alpha_i \rho C_A \gamma_A \frac{M_i}{M_A} \sqrt{\frac{kT_W}{2\pi M_A}} \quad (10)$$

The most important point to make about this model is that the introduction of the surface mass of the TPS must induce a wall-normal velocity that is tightly coupled to the mass diffusion rates. The capability for blowing has already been demonstrated in §III, but this model creates additional coupling of the surface system blowing to the surface system composition. The total mass blowing contribution from an arbitrary number of reactions of this type is given in Eqn (11), where the value of $M_{S,k}$ is determined from stoichiometry of the gas phase participants in each reaction.

$$\dot{m} = \rho v_W = \sum_k \rho C_{A,k} \gamma_{A,k} \frac{M_{S,k}}{M_{A,k}} \sqrt{\frac{kT_W}{2\pi M_{A,k}}} \quad (11)$$

B. Example using Park Graphite Model

An example case was selected from the work of Chen and Milos²⁸ that is a graphite cone tested in an arc facility. The model is a 10° half-angle shape with a nose radius of 1.905-cm. Test conditions were given by them as $U = 5.354$ km/s, $\rho = 0.003$ kg/m³, $T = 1428$ K, $C_{O_2}=0.0$, $C_{N_2}=0.6169$, $C_{NO}=0.0046$, $C_N=0.1212$, $C_O=0.2573$. The gas/surface interaction model employed in their calculation was that of Park²⁷, which includes up to four reactions governing the mechanisms of carbon oxidation (via atomic and molecular oxygen), nitridation, and sublimation. They used the Navier-Stokes code GIANTS²⁹, which does share some heritage with the DPLR code. Despite this, some details of their analysis were not readily available such as reaction rates for the finite rate chemical reactions, assumptions about vibrational excitation, and most importantly, the emissivity coefficient of the radiating graphite wall. Reasonable values were assumed for these things from DPLR's available database and the flowfield was computed so that at least a qualitative comparison could be made to their results for verification of the gas/surface model implementation. The grid used and the resulting flowfield is shown in Fig 20.

The predicted heat transfer profile is plotted in Fig 21 and the mass blowing rate is plotted in Fig 22 for this case. The magnitude of the results agrees very favorably with the results obtained by Chen and Milos for this case to within the error of the assumptions made in the analysis. The result is also quite sensitive to the gas diffusion model since this directly impacts the amount of oxidizer that reaches the surface. Chen and Milos also showed this with several diffusion models in GIANTS, but the overall band of the results is about the same from both analyses.

The stagnation point heat transfer from Fig 21 is predicted to be a maximum of approximately 1.10 kW/cm^2 , which is considerably lower than the 1.91 kW/cm^2 predicted from the super-catalytic, non-blowing case. It may be inferred therefore that the super-catalytic, non-blowing model will result in a significant over-design of the vehicle TPS system. Therefore, this model provides a simple, first-order mechanism to assess the impact of gas/surface interaction on the aerothermal environment of a vehicle. More importantly, the analysis employing the modified DPLR code introduced no destabilizing numerical stability or convergence effects by coupling the blowing and species rate production terms at the gas/surface interface.

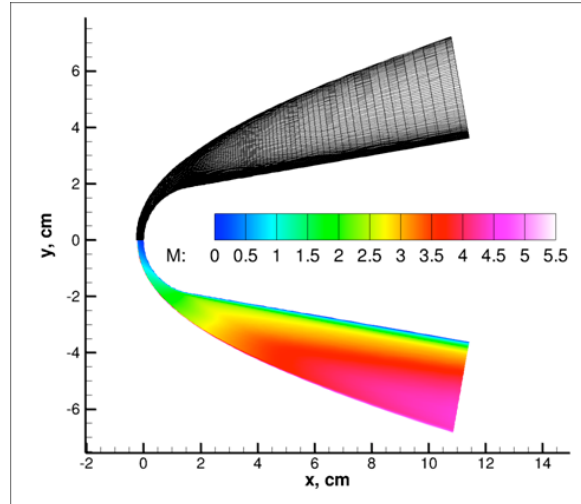


Figure 20. Grid and Flowfield from Test Case of Chen and Milos²⁸

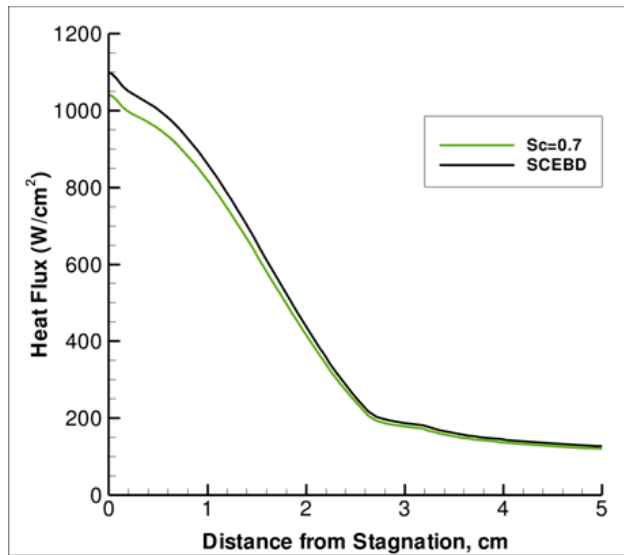


Figure 21. Predicted Surface Heat Flux with Diffusion-Limited Oxidation Model

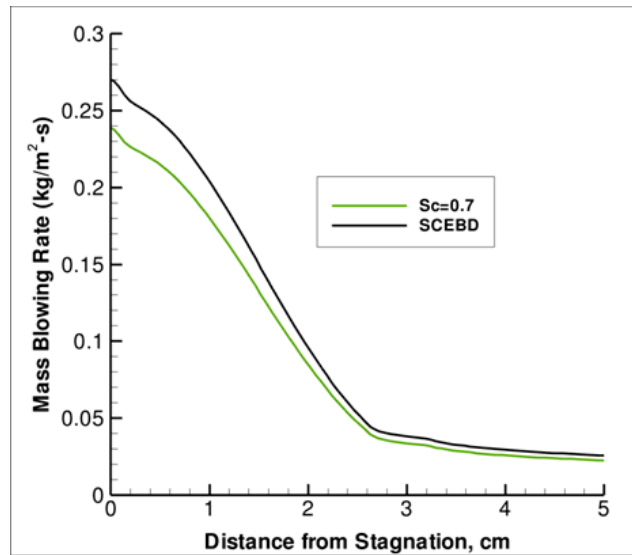


Figure 22. Predicted Surface Mass Blowing Flux with Diffusion-Limited Oxidation Model

C. Oxidation Limited Diffusion of Fiberform

A series of relevant cases using this diffusion-limited oxidation model that has been implemented in the DPLR code have also been published by Driver, et al³⁰. They used the diffusion-limited oxidation boundary condition to explain unexpectedly high recession rates observed in a series of tests of PICA and fiberform (PICA without phenolic). Uncoupled analysis with CFD and material response under-predicts the measured experimental recession rates for fiberform by a factor of as much as 2.5 times. Since the main ablation mechanism of fiberform under the range of conditions studied is the formation of carbon monoxide by oxidation, the diffusion limited oxidation boundary condition was utilized with a single reaction forming carbon monoxide from atomic oxygen. This model significantly reduced the uncertainty in predicting the measured data for such heat shields. Interested readers are encouraged to consult the publication of Driver, et al³⁰ for details and predicted recession rates that are compared to the experiments.

VI. Conclusions

Three surface boundary conditions have been incorporated into the DPLR thermo-chemically reacting CFD code. These boundary conditions have been implemented to simulate various aspects of integrated surface and material response for thermal protection system applications. The surface blowing boundary condition, which was in place in the code prior to this effort, has been modified to improve the implicit boundary condition coupling and accelerate convergence for injection of gases that are not a dominant constituent of the freestream. This capability was demonstrated on a generic cone problem and it was found that the blowing boundary condition converged at a rate that was on the same order or magnitude as a similar non-blowing case. Comparisons were made to several cases where experimental heat transfer was measured on a 5° cone with distributed blowing with several gases. It was found in making these comparisons that extracting the total viscous energy flux, where this term includes both thermal and diffusion gradient components, resulted in significant discrepancies with the measurements for injectant gases that had a different specific enthalpy than the air diffusing to the surface. After additional analysis, it was discovered that comparing the measured heat transfer to the thermal heat flux resulted in significantly improved comparisons to the measured data. The cause for this was presumed to be due to the fact that the injectant gas passes through the surface from the reservoir and into the flow without exchanging energy with the solid surface of the model.

An equilibrium boundary condition has also been demonstrated where the composition of the gas at each surface location is fixed by Gibbs free-energy minimization using an energy minimization technique that is compatible with the NASA CEA code. The boundary condition is enforced implicitly by employing the free-energy minimization system to compute derivative with respect to the surface and near-surface diffused quantities to maintain stability. With careful CFL ramping during the early stage of convergence where large transients occur, the boundary condition was found to converge at similar rates as non-catalytic boundaries do. Several test cases were demonstrated that show the boundary predicts equilibrium composition that exactly matches the CEA results at each point where the surface temperature is high enough to partially dissociate the flow. For conditions where the surface is cold enough to prefer complete recombination, the equilibrium boundary enforces this naturally without explicit intervention from the user. For certain systems, the predicted heating patterns can result in significant TPS savings over super-catalytic recombination.

Finally, a somewhat-general, diffusion-limited oxidation style boundary was coded to allow surface consuming reactions such as the oxidation of carbon to release carbon monoxide. This boundary condition enforces catalytic source terms in the surface boundary and incorporates implicitly coupled blowing at the surface to maintain mass balance from the consumed reactant. This type of boundary condition has been used to compare to existing cases with another implementation of a similar model and more importantly to improve prediction of a series of arcjet test cases where recession rate was measured. The reduction in uncertainty prediction has a direct impact on reducing the margins of current NASA missions such as MSL and CEV Orion.

Each of these three boundary conditions may be considered simplified steps to modeling integrated material response. The key result from the implementation of these three simplified boundaries has been the process of implicitly coupling the dependencies of the boundary conditions into the solver to maintain stability of the code without sacrificing convergence rate. These lessons learned will be applied to more complex, integrated boundaries for future improvements to the modeling of surface material response.

VII. Acknowledgement

This work was paid for by grant #NNX08AZ43G funded by NASA Ames Research Center.

VIII. References

¹Wright, M.J.; Bose, D.; and Candler, G.V. "A Data Parallel Line Relaxation Method for the Navier-Stokes Equations". *AIAA Journal*. Vol 36, no 9. Pgs 1603 – 1609. Sept 1998.

²MacCormack, R.W. and Candler, G.V. "The Solution of the Navier-Stokes Equations Using Gauss-Seidel Line Relaxation". *Computers and Fluids*. Vol 17, No 1. Pgs 135 – 150. 1989.

³Candler, G.V. "Chemistry of External Flows". *Aerothermochemistry for Hypersonic Technology*: Von Karman Institute for Fluid Dynamics Lecture Series. VKI LS 1995-04.

⁴Landau, L. and Teller, E. "Theory of Sound Dispersion". *Physikalische Zeitschrift der Sowjetunion*. Vol 10, no 34. 1936.

⁵Millikan, R. and White, D. "Systematics of Vibrational Relaxation". *Journal of Chemical Physics*. Vol 39, no 12. Pgs 3209 – 3213. 1963.

⁶Camac, M. "CO₂ Relaxation Processes in Shock Waves". *Fundamental Phenomena in Hypersonic Flow*. J.G. Hall Ed. Cornell University Press. Pgs 195 – 215, 1964.

- ⁷Park, C.; Howe, J.T.; Jaffe, R.J.; and Candler, G.V. "Review of Chemical-Kinetic Problems of Future NASA Missions II: Mars Entries". *Journal of Thermophysics and Heat Transfer*. Vol 8, no 1. Pgs 9 – 23. 1994.
- ⁸Park, Chul. "Assessment of Two-temperature Kinetic Model for Ionizing Air". AIAA Paper 87-1574. AIAA 22ND Thermophysics Conference. Honolulu, HI: 8-10 June 1987.
- ⁹Marrone, P.V. and Treanor, C.E. "Chemical Relaxation with Preferential Dissociation from Excited Vibrational Levels". *The Physics of Fluids*, Vol 6, no 9. Pgs 1215 – 1221. September 1963.
- ¹⁰Palmer, G.E. and Wright, M.J. "A Comparison of Methods to Compute High Temperature Gas Viscosity". *Journal of Thermophysics and Heat Transfer*. Vol 17, no 2. Pgs 232 – 239. 2003.
- ¹¹Palmer, G.E. and Wright, M.J. "A Comparison of Methods to Compute High Temperature Gas Thermal Conductivity". AIAA Paper 2003-3913. Jun 2003.
- ¹²Gupta, R.; Yos, J.; Thompson, R.; and Lee, K. "A Review of Reaction Rates and Thermodynamic and Transport Properties for an 11-Species Air Model for Chemical and Thermal Nonequilibrium Calculations to 30000 K". NASA RP-1232. August 1990.
- ¹³Ramshaw, J.D. "Self-consistent Effective Binary Diffusion in Multicomponent Gas Mixtures". *Journal of Non-Equilibrium Thermodynamics*. Vol 15, no 3. Pgs 295 – 300. 1990.
- ¹⁴Baldwin, B.S. and Lomax, H. "Thin Layer Approximation and Algebraic Model for Separated Turbulent Flows". AIAA Paper 78-0257. Huntsville, AL: 1978.
- ¹⁵Spalart, P.R. and Allmaras S.R. "A One-Equation Turbulence Model for Aerodynamic Flows". AIAA Paper 92-0439. 30TH Aerospace Sciences Meeting & Exhibit. Reno, NV: 6-9 Jan, 1992.
- ¹⁶Menter, F.R. "Two-Equation Eddy-Viscosity Turbulence Models for Engineering Applications". *AIAA Journal*. Vol 32, no 8. Pgs 1598 – 1605. August 1994.
- ¹⁷Brown, James. "Turbulence Model Validation for Hypersonic Flow". AIAA Paper 2002-3308. 8TH Thermophysics and Heat Transfer Conference. St. Paul, MN: 24 – 26 Jun 2002.
- ¹⁸Catris S. and Aupoix B. "Improved Turbulence Models for Compressible Boundary Layers." AIAA Paper 98-2696. 2ND Theoretical Fluid Mechanics Meeting: Albuquerque, NM, June 1998.
- ¹⁹Saunders, D.; Yoon, S.; and Wright, M. "An Approach to Shock Envelope Grid Tailoring and Its Effect on Reentry Vehicle Solutions." AIAA Paper 2007-0207. 45TH Aerospace Sciences Meeting & Exhibit. Reno, NV: 8-11 January 2007.
- ²⁰Thompson, R.A. and Gnoffo, P.A. "Implementation of a Blowing Boundary Condition in the LAURA Code." AIAA Paper 2008-1243. 46TH Aerospace Sciences Meeting & Exhibit. Reno, NV: 7-10 January 2008.
- ²¹Gnoffo, Peter A.; Johnston, Christopher O.; and Thompson, Richard A. "Implementation of Radiation, Ablation, and Free-energy Minimization Modules for Couples Simulations of Hypersonic Flow." AIAA Paper 2009-1399. 47TH Aerospace Sciences Meeting & Exhibit. Orlando, FL: 5-8 January 2009.
- ²²Martin, Alexandre and Boyd, Iain D. "Implicit Implementation of Material Response and Moving Meshes for Hypersonic Re-entry Ablation." AIAA Paper 2009-0670. 47TH Aerospace Sciences Meeting & Exhibit. Orlando, FL: 5-8 January 2009.
- ²³Nompelis, I.; Candler, G.; and Conti, R.J. "A Parallel Implicit CFD Code for the Simulation of Ablating Re-entry Vehicles." AIAA Paper 2009-1562. 47TH Aerospace Sciences Meeting & Exhibit. Orlando, FL: 5-8 January 2009.
- ²⁴Marvin, Joseph G. and Akin, Clifford, M. "Combined Effects of Mass Addition and Nose Bluntness on Boundary-Layer Transition." *AIAA Journal*. Vol 8, No 5. Pgs 857 – 863. May 1970.
- ²⁵Gordon, S. and McBride, B. "Computer Program for Calculation of Complex Chemical Equilibrium Compositions and Applications." NASA RP-1311. October 1994.
- ²⁶Titov, E.V.; Levin, D.A.; Picetti, D.J.; and Anderson, B.P. "Simulation of TPS Crack Growth Due to Carbon Oxidation Using Advanced Grid Morphing Techniques." AIAA Paper 2009-3599. 41ST AIAA Thermophysics Conference. San Antonio, TX: 22-25 June 2009.
- ²⁷Park, Chul. "Stagnation-Point Ablation of Carbonaceous Flat Disks – Part I: Theory." *AIAA Journal*, Vol 21, no 11. Pgs 1588 – 1594. Nov 1983.
- ²⁸Chen, Yih-Kanq and Milos, Frank S. "Finite-Rate Ablation Boundary Conditions for a Carbon-Phenolic Heat-Shield." AIAA Paper 2004-2270. 37TH AIAA Thermophysics Conference. Portland, OR: 28 June-1 July 2004.
- ²⁹Candler, G.V. "The Computation of Hypersonic Ionized Flows in Chemical and Thermal Nonequilibrium." AIAA Paper 88-0511, January 1988.
- ³⁰Driver, D.; Olsen, M.; Barnhardt, M.; and MacLean, M. "Understanding High Recession Rates of Carbon Ablators Seen in Shear Tests in an Arc Jet." AIAA Paper 2010-1177. 48TH Aerospace Sciences Meeting & Exhibit. Orlando, FL: 4-7 January 2010.